CONDENSED MATTER PHYSICS

Disentangling the intertwined orders in a magnetic kagome metal

Ji Seop Oh[1,2,3,4], Ananya Biswas[2], Mason L. Klemm[2], Hengxin Tan[5], Yaofeng Xie[2], Bin Gao[2], Makoto Hashimoto[6], Donghui Lu[6], Binghai Yan[5,7], Pengcheng Dai[2], Robert J. Birgeneau[1,8]*, Ming Yi[2]*

Intertwined orders appear when multiple orders are strongly interacting, and kagome metals have emerged as new platforms to explore exotic phases. FeGe has been found to develop a charge density wave (CDW) order within magnetic phase, suggesting an intricate interplay of the lattice, charge, and spin degrees of freedom. Recently, postgrowth annealing has been proposed to tune the CDW order from long-range to complete suppression, offering a tuning knob for the CDW order. Here, by comparing the electronic structures of FeGe subjected to different annealing conditions and distinct CDW properties, we report spectral evolution associated with the lattice and spin degrees of freedom. We find band evolution linked to a spin density wave (SDW) order present in both samples with and without CDW order, and another evolution connected to the lattice distortions that onset with the long-range CDW order and revert with the SDW order. Our results reveal a rare competitive cooperation of the lattice, spin, and charge in FeGe.

INTRODUCTION

Intertwined orders refer to phenomena often found in correlated electron systems, where distinct broken symmetry phases driven by distinct degrees of freedom appear in either a competitive or cooperative relationship due to the intricate balance of energy scales. Intertwined orders are often found in the phase diagram of unconventional superconductors such as the cuprates and the iron pnictides (*1*). For example, in the iron-based superconductors, the strong intertwinement of the orbital and spin degrees of freedom leads to two strongly coupled order parameters manifested as the nematic order and the spin density wave (SDW) order, the suppression of which leads to superconductivity. In these systems, the presence of electronic instabilities near the Fermi level (E_F) can further contribute to the interplay of the different degrees of freedom and lead to exotic phases (*2*–*4*).

A recent example of these emergent orders are seen in metallic kagome lattices (*5*–*20*), where the chemical potential resides near saddle points in the electronic structures or Van Hove singularities (VHSs). Theoretical models, considering intra- and intersite Coulomb interactions, predict distinctive charge density wave (CDW) phases characterized by nonzero angular momentum of a particle-hole pair (*7*, *10*). This has been further suggested to indicate the existence of orbital loop currents and nematicity (*10*, *21*), differentiating the CDW order in this material from ordinary charge ordering. One system that embodies this prediction is the vanadium-based kagome lattice AV_3Sb_5 (A = Cs, K, and Rb) (*8*–*20*), where CDW order with broken time-reversal symmetry (*16*) and superconductivity have been reported (*9*). However, in this system, it is the electronic and lattice degrees of freedom that drive the ordered phases, as there is no reported magnetism.

Mn- or Fe-based metallic kagome magnets introduce the magnetic degree of freedom to the emergent kagome physics (*22*). FeGe, an A-type antiferromagnet whose onset temperature is at 410 K (*23*, *24*), stands out as a special example among the kagome magnets. Structurally, it has been identified as a fundamental building block of these kagome magnets based on an advanced kagome effective Hamiltonian using a *d*-orbital basis (*25*). It is also known because of its unique CDW phase below 110 K (T_{CDW}) that appears in an ordered magnetic phase (*26*–*32*). Furthermore, theoretical frameworks have been established to explain the exotic ground state of FeGe in broader contexts. In the magnetic phase diagram based on a Hartree-Fock approach, FeGe is located at the boundary of spatial stripe spin-charge order (*29*). Consequently, FeGe has garnered substantial attention, offering a unique platform to study interplay between the CDW order and magnetism. A dimerization of one-fourth of the Ge sites have been reported to play a major role in establishing the CDW order, indicating the importance of the lattice degree of freedom (*33*, *34*). In addition, recent reports indicate that postgrowth annealing is highly effective at tuning the CDW order; namely, the annealing temperature can tune the short-range CDW order in the as-grown crystals either to a long-range order or completely suppressed by controlling the redistribution of the lattice disorder in the form of Ge vacancies—disrupting Ge dimer and CDW formation or precipitating them, in turn enabling stoichiometry restoration and long-range CDW order (*35*–*40*). The postgrowth annealing, therefore, provides a unique tuning knob for understanding the intricate balance of energy scales that determine the ordered phases in FeGe.

Here, we present a systematic study of the temperature-dependent electronic structures of FeGe annealed under 320°C (FG320) and 560°C (FG560), with long-range CDW order present in FG320 and absent in FG560. We first provide clear spectral contrast between the long-range CDW order in FG320 and the absence of such

[1]Department of Physics, University of California, Berkeley, CA 94720, USA. [2]Department of Physics and Astronomy and Smalley-Curl Institute, Rice University, Houston, TX 77005, USA. [3]Department of Applied Physics, Sookmyung Women's University, Seoul 04310, Republic of Korea. [4]Institute of Advanced Materials and Systems, Sookmyung Women's University, Seoul 04310, Republic of Korea. [5]Department of Condensed Matter Physics, Weizmann Institute of Science, Rehovot 7610001, Israel. [6]Stanford Synchrotron Radiation Lightsource, SLAC National Accelerator Laboratory, Menlo Park, CA 94025, USA. [7]Department of Physics, The Pennsylvania State University, University Park, PA 16802, USA. [8]Materials Science Division, Lawrence Berkeley National Laboratory, Berkeley, CA 94720, USA.
*Corresponding author. Email: mingyi@rice.edu (M.Y.); robertjb@berkeley.edu (R.J.B.)

in FG560 in the form of CDW gap formation on the VHS-forming band dispersion. We find a band evolution indicative of an SDW order that is present in both compounds, with a higher transition temperature, T_{SDW}, in FG320 in the presence of long-range CDW order. Unexpectedly, we find the CDW gap to be enhanced below T_{SDW}. In addition, we observe a distinct band evolution that onsets at T_{CDW} and is reversed at the lower T_{SDW} in FG320, which can only be ascribed to an electronic response to the Ge dimerization in the lattice at T_{CDW} that is subsequently reverted at T_{SDW}. Taking all observations together, we reveal an intricate interplay of the lattice, charge, and spin degrees of freedom tuned by postgrowth annealing: The Ge dimerization and associated lattice distortions are initially necessary for the formation of the CDW order. However, at a lower temperature within the CDW order, an SDW order disrupts the strong coupling of the Ge dimerization and the CDW order, results in the reversal of the electronic response to the lattice distortion, and further enhances the CDW order. Our observations, together, reveal a highly unusual intertwinement of the lattice, spin, and charge degrees of freedom: The Ge dimerization (lattice) and the SDW formation (spin) each appear to be strongly coupled to the CDW order yet compete with each other to stabilize and accompany the long-range CDW order. This highly unusual "competitive cooperation" of the three distinct degrees of freedom is quite rare among correlated materials and reveals very close energy scales that lead to the highly tunable nature of the ground states of this kagome magnet.

RESULTS

Characterizations for annealed FeGe crystals

As shown in Fig. 1A, the crystal structure of kagome FeGe consists of alternating Fe kagome layer and Ge honeycomb layer along the *c* axis. In accordance with previous reports, we annealed our crystals at either 320° or 560°C for 96 hours for inducing long-range CDW order in the former and suppressing CDW order in the latter, which we label as FG320 and FG560, respectively. The effects on the phases in FG320 and FG560 are presented in Fig. 1B, consistent with previous reports (*35*, *36*). Both FG320 and FG560 have similar T_N of 410 K. Our magnetic susceptibility measurements on the two types of crystals show the sharp CDW order in FG320 and the lack of this anomaly in FG560, as presented in Fig. 1C, similar to previous reports showing high sensitivity to annealing conditions (*36*, *37*, *39*, *40*). In addition, a magnetic transition also appears in FG320 within the CDW-ordered phase. Previously, this transition was interpreted as a spincanting transition and denoted in the literature as $T_{canting}$. However, recent inelastic neutron scattering experiments have demonstrated that spin canting of local moments cannot be the correct magnetic ground state associated with this transition. Instead, the magnetic order must be an itinerant SDW order that onsets at this transition (*31*, *40*). Hence, we label this transition as T_{SDW} instead of $T_{canting}$ throughout the manuscript. As will be discussed later and also demonstrated by recent neutron scattering measurements (*40*), such a temperature scale is also observed for FG560, albeit at a lower temperature.

Comparisons of electronic structures between FG320 and FG560

Now, we compare the electronic structures of FG320 and FG560 as measured by angle-resolved photoemission spectroscopy (ARPES).

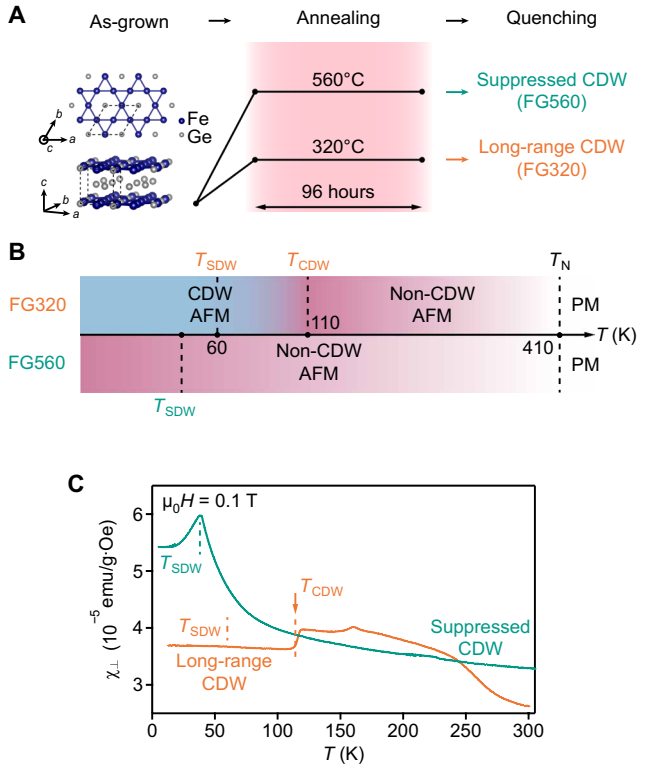

Fig. 1. Characterizations for long-range and suppressed CDW order. (**A**) Crystal structure of FeGe from top and side perspectives. Postannealing conditions for achieving long-range (FG320) or suppressed (FG560) CDW order are shown. (**B**) Schematic illustration for the distinct phases in FG320 and FG560 as a function of temperature. PM, paramagnetic phase. (**C**) Magnetic susceptibility with field perpendicular to the (001) direction.

Since the valence band is dominated by the Fe 3*d* orbitals forming a layered kagome network, we use the surface Brillouin zone (BZ) notations for simplicity, as shown in Fig. 2A. An empirical schematic of the valence band is presented in Fig. 2B, where we use the notations of VHS1 and VHS2 to label the VHSs of dominantly $d_{x^2-y^2}/d_{xy}$ orbitals and d_{xz}/d_{yz} orbitals, respectively, in accordance with previous work (*28*). Note that these band dispersions are likely bulk states, as they are observed regardless of surface termination after cleavage. We first directly compare the measured Fermi surfaces (FSs) of FG320 and FG560 both above and below T_{CDW}. The top half of Fig. 2C shows the FSs of FG320, while the bottom half shows the FSs of FG560. The left half of Fig. 2C shows the FSs measured below T_{CDW} at 80 K on the two samples, while the right half shows the measurement at 150 K above T_{CDW}. All measurements were carried out under identical photon energy and polarization. First, at 150 K, the FSs of FG320 and FG560 appear to be very similar. Of the four quadrants, only the top left quadrant is obtained in a phase with long-range CDW order. Comparing these data with the others, we identify two main distinctions. First, the spectral intensity between $\overline{K}$ and $\overline{M}$ (marked by an orange rectangle) is suppressed in the CDW state, while it is noticeable in all other states. This is consistent with the suppression of spectral weight due to the opening of a CDW gap on the VHSs at $\overline{M}$. Second, we observe a change in the appearance of the circular FS near the $\overline{\Gamma}$

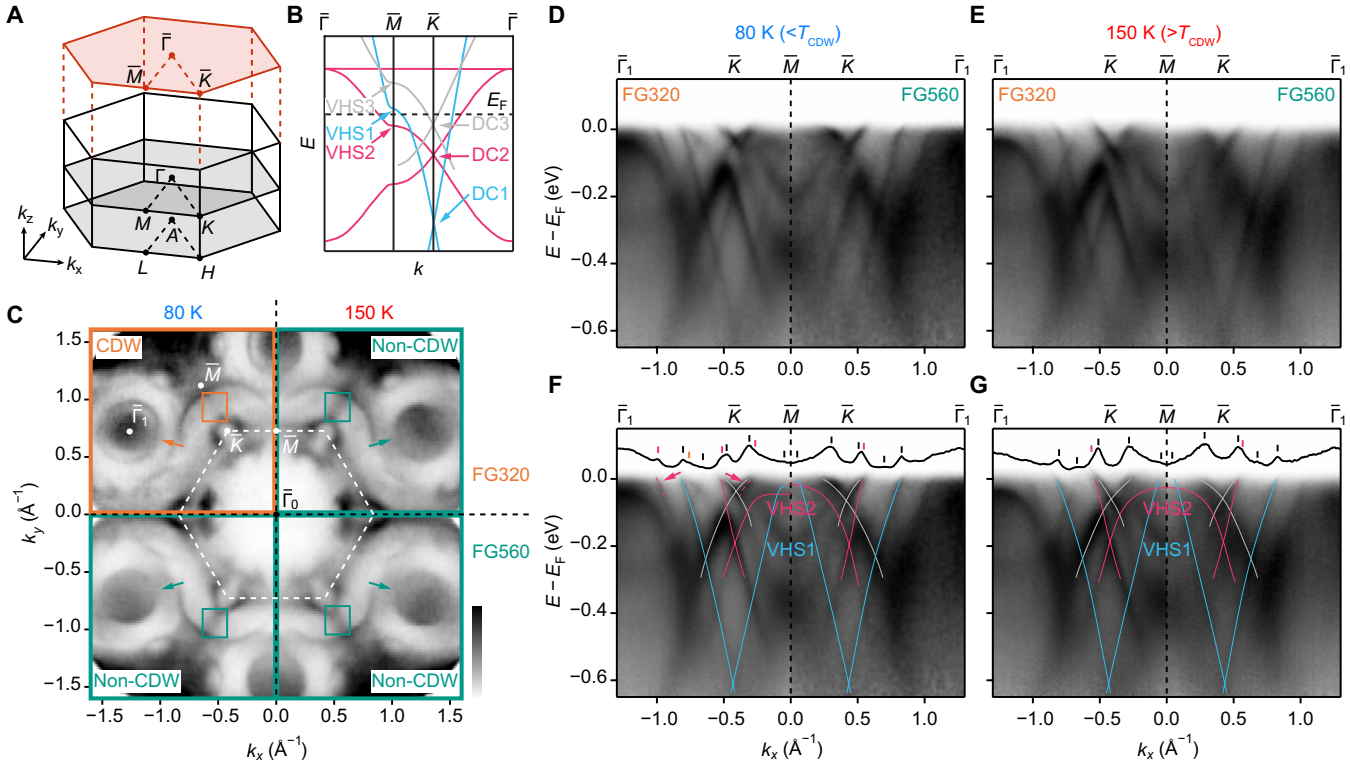

Fig. 2. Comparison of electronic structures between FG320 and FG560 below and above T_{CDW}. (**A**) Brillouin zone and locations of high-symmetry points of FeGe. Surface-projected Brillouin zone is also depicted. (**B**) Schematic band dispersions for FeGe. (**C**) FS maps obtained from FG320 (top) and FG560 (bottom) at 80 K ($<T_{CDW}$; left) and 150 K ($>T_{CDW}$; right), as plotted in the four quadrants. Orange and green arrows/boxes mark distinct features when comparing CDW-ordered and normal phases. (**D**) A side-by-side comparison of band dispersions along the $\overline{K}$-$\overline{M}$-$\overline{K}$ between FG320 and FG560 at 80 K. (**E**) Similar comparison at 150 K. (**F**) Same plot as (D) with guides for the eye to trace VHS1 and VHS2 band dispersions. MDC at E_F is overlaid showing peak locations of E_F-crossing band dispersions. We mark peak locations with green bars and differentiate extra bands in the CDW phase with orange bars. (**G**) Same plot as (F) but for 150 K. Note that no extra band crossing at E_F is observed. All measurements are taken with 69-eV photons.

point, which is reproduced by bulk density functional theory calculations in the pristine (non-CDW) case and in the CDW phase by a recent work assuming a disordered distribution of Ge dimers (*38*, *41*). This is more apparent in the second BZ ($\overline{\Gamma}_1$) due to less suppression by photoemission matrix elements. Noticeably, the circular pocket is separated from the broad spectral intensity only in the CDW phase. We infer that it may come from orbital-dependent band shifts. Note that the FSs in the non-CDW phase are invariant under different postannealing conditions, implying that the suppression of the CDW order is intrinsic and not due to sample quality variation.

Next, we present a side-by-side comparison of band dispersions measured along the $\overline{K}$-$\overline{M}$-$\overline{K}$ high-symmetry cuts. Figure 2 (D and E) shows raw ARPES intensity plots at 80 and 150 K from FG320 (left half in each plot) and FG560 (right half in each plot). Figure 2 (F and G) shows the same data but overlaid with the corresponding momentum distribution curves (MDCs) at E_F and guidelines using annotations from Fig. 2B. Again, very little difference is observed on the band dispersions of the two samples at 150 K, but additional bands from band folding are observed in the 80-K data for FG320. This is further supported by peaks found in the MDCs (pink and orange bars) in the CDW phase in addition to those found in the non-CDW phase (black bars) (Fig. 2F). These additional band dispersions are also shown by dashed lines and pink arrows.

CDW gap

We further differentiate FG320 and FG560 directly by examining the CDW gap as a function of temperature. For FG320, from the side-by-side comparison of the dispersions along the $\overline{K}$-$\overline{M}$-$\overline{K}$ at 15 and 150 K, spectral weight near E_F is suppressed between $\overline{K}$ and $\overline{M}$ in the CDW phase, consistent with the observation on the FS maps. More details can be observed from the temperature dependence of the energy distribution curves (EDCs) at two different Fermi momenta, k_{VHS} and k_0, defined as the momenta where the bands corresponding to VHS1 and VHS3 cross E_F. The Fermi-Dirac (FD) distribution function has been divided from all the EDCs. As the location of both k_0 and k_{VHS} vary with temperature (to be discussed in the following section), the EDC at each temperature is taken after precisely determining the momentum of the band crossing at each temperature. From the temperature dependence of FD-divided EDCs at k_{VHS} (Fig. 3, B and C), indications of a gap opening below T_{CDW} can be identified as both changes in the slopes near E_F (black arrows) and the presence of dips in the intensity, both disappearing near T_{CDW}. In contrast, the EDCs at $k = k_0$ show peaks at E_F for all temperatures, demonstrating the absence of a CDW gap. Both observations of the presence and absence of the CDW gap at k_{VHS} and k_0, respectively, are consistent with momentum-dependent CDW gap opening characterized in the as-grown FeGe. The temperature evolution of the CDW gap can also be visualized from symmetrized

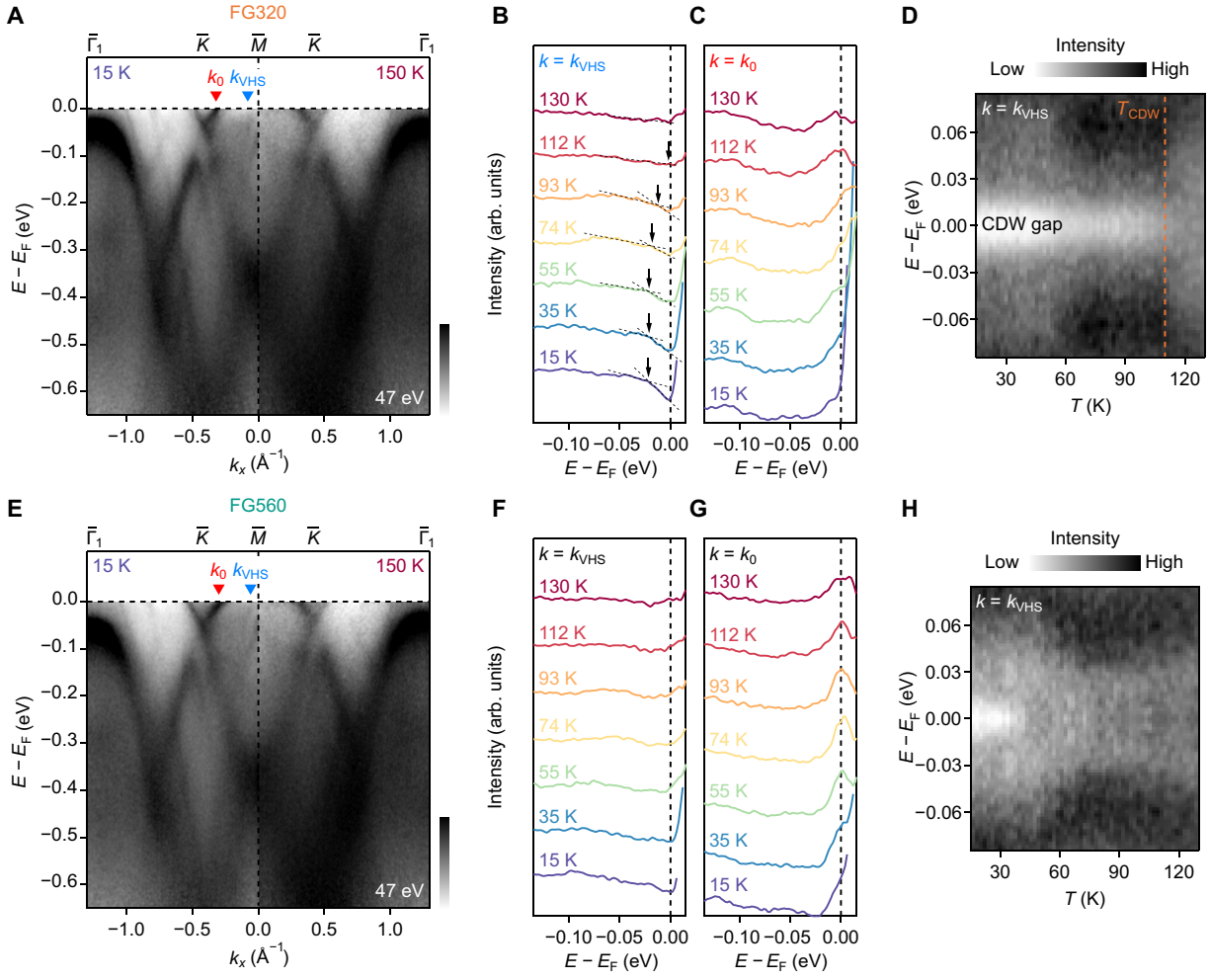

Fig. 3. CDW gap in FG320 and FG560. (**A**) A side-by-side comparison of band dispersions from FG320 along the $\overline{K}$-$\overline{M}$-$\overline{K}$ taken at 15 K (left) and 150 K (right). Two representative Fermi momenta are annotated as k_{VHS} and k_0. (**B**) EDCs at various temperatures obtained at k_{VHS} as marked in (A). We divided out the FD distributions from all the EDCs, revealing a dip feature near E_F below T_{CDW} (=110 K). Arrows point at where the dashed guidelines cross, which indicates a slope change in the EDCs as the CDW gap opens. (**C**) Same plot as (B) obtained at k_0. Contrary to (B), we observe peaks at E_F at all temperatures. (**D**) Stacked plots of symmetrized EDCs at k_{VHS}. The white region shows where spectral intensity is suppressed, corresponding to the CDW gap region. (**E** to **H**) Analogous plots to (A) to (D) from FG560. Note that CDW gap is not as evident as it is in FG320. Smaller white region in (H) than that in (D) is from suppressed CDW order. All measurements are taken with 69-eV photons.

EDCs at k_{VHS} (Fig. 3D), which show suppressed intensity at E_F that closes around $T_{CDW} = 110$ K. We note that to capture the subtle gap opening effect, we used the continuous ramping method of taking measurements while very slowly ramping the sample temperature. This method is effective at capturing subtle spectral changes and identifying phase transitions. We note that the CDW gap is only observed on selected bands with a gap size of 20 meV, while most band crossings remain gapless. Hence, it remains to be seen the expected effect of such a momentum-dependent gap by optical spectroscopy in the corresponding energy range, which is from the joint density of states over the entire BZ (*34*, *42*).

Via the same method, we can examine the temperature evolution of the possible CDW gap in FG560, where no clear long-range CDW characteristic is observed in the magnetic susceptibility measurement. Contrary to FG320, the band dispersions at 15 and 150 K in FG560 show no obvious differences in the spectral intensity at E_F between $\overline{K}$ and $\overline{M}$ (Fig. 3E). FD-divided EDCs at k_{VHS} and k_0 shown in Fig. 3 (F and G) provide noticeable differences from those of FG320. Signatures of the CDW gaps in Fig. 3F are almost absent except for small dip-like features below 35 K. All the EDCs shown in Fig. 3G show peaks at E_F and similar temperature dependence with that shown in Fig. 3C. In the symmetrized EDC spectral image shown in Fig. 3H, we identify a smaller white region than that for FG320, indicating much weaker CDW nature in FG560. We propose that this weak spectral weight suppression for a limited temperature window may be from fluctuating short-range CDW order. A detailed comparison of the EDCs for the two types of samples is also provided in the Supplementary Materials.

Temperature evolution of the electronic structures

Now, we compare the temperature dependence of the band dispersions of FG320 and FG560. The temperature-dependent dispersions measured along the $\overline{K}$-$\overline{M}$-$\overline{K}$ high-symmetry cut are shown for FG320 in Fig. 4A. Here, in addition to VHS1 and VHS2, we also

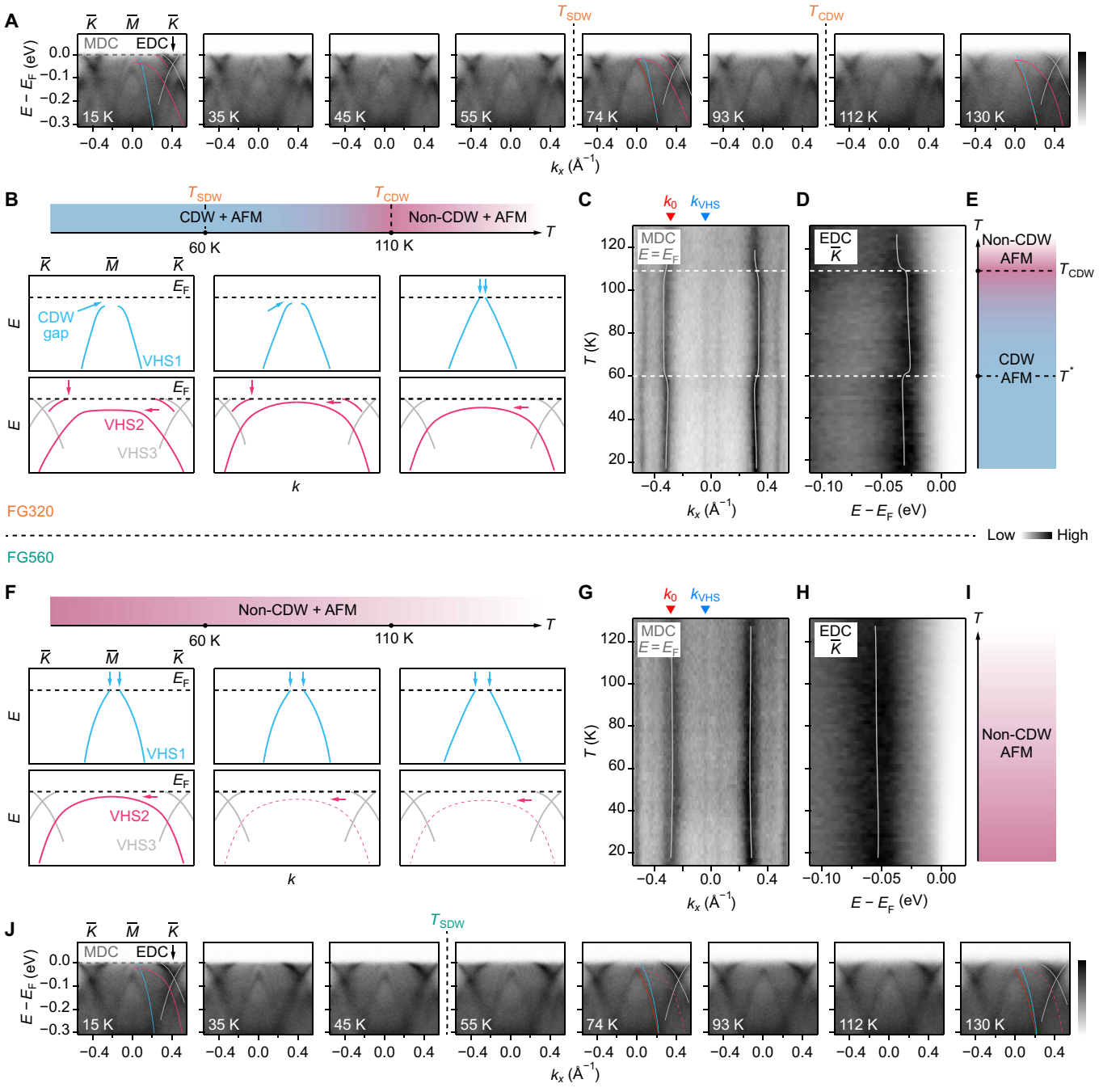

Fig. 4. Band dispersions at representative temperatures and their evolutions in FG320 and FG560. (**A**) High-symmetry cuts along the $\overline{K}$-$\overline{M}$-$\overline{K}$ at representative temperatures from FG320. T_{SDW} and T_{CDW} are indicated. MDC (gray dashed line) and EDC (black arrow at $k_x = \overline{K}$) are locations where we take a stack MDCs shown in (C) and two stacks of EDCs in (D). (**B**) Schematics showing how band dispersions evolve as a function of temperature. Notable energy and momentum locations are pointed by colored arrows. Phase indicator bar is put together above the schematics, matching the horizontal temperature scale. (**C**) A stacked MDC at E_F, showing nonmonotonic temperature evolutions of Fermi momenta across T_{SDW} (=60 K) and T_{CDW} (=110 K). (**D**) A stacked EDC at $\overline{K}$, which presents the band shift across T_{CDW} and a reverted behavior at T_{SDW}. (**E**) Phase indicator whose temperature axis is aligned with (C) and (D). (**F** to **I**) Analogous plots to (B) to (E) from FG560. (**J**) High-symmetry cuts along $\overline{M}$ and $\overline{K}$ at representative temperatures from FG560. All measurements are taken with 47- eV photons.

label VHS3, which is driven by d_{z^2} orbital. The changes across temperature can be better visualized by the spectral images made from the temperature dependence of the MDC taken at E_F (Fig. 4C) and the EDC taken at the $\overline{K}$ point (Fig. 4D). We emphasize again that these measurements were taken by the ramping method of continuous data acquisition while very slowly ramping the sample temperature, which is an effective method for tracking subtle spectral changes as a function of temperature. The most prominent feature captured by these images is the Dirac band that crosses E_F at $\overline{K}$, with k_0 as the Fermi momentum shown in the MDC stack and the Dirac point shown in the EDC stack. Notably, as temperature is lowered across T_{CDW}, k_0 shifts toward $\overline{K}$ captured by the MDC image, consistent with an upshift of this band in energy also seen by the EDC image. This shift is reversed when temperature is lowered across T_{SDW}. In a previous ARPES report on an annealed FeGe, this shift is observed across T_{CDW} and was interpreted to be a manifestation of the lattice changes associated with the Ge dimerization based on density functional theory calculations (*38*). In addition, below T_{SDW}, a monotonic energy shift as a function of temperature is observed, which is due to the increase in the total magnetic moment at the onset of the SDW order as will be discussed later (*28*). We summarize the band evolution with the schematic in Fig. 4B, which includes the CDW gap formation on the VHS1-forming band below T_{CDW} and the back bending of the VHS2-forming band and its shift across T_{SDW} and T_{CDW}.

In comparison, we show the exact same measurements on FG560, where the temperature evolution can be visualized via the MDC and EDC stacks (Fig. 4, G to J). VHS2 has only one band near E_F, implying that back bending and doubling of VHS2 are absent in FG560. The VHS2-forming band dispersion becomes broad and fades above T_{SDW} in FG560. In contrast to FG320, the Dirac band shift at $\overline{K}$ between T_{SDW} and T_{CDW} is not observed in FG560. No noticeable change occurs above $T_{SDW} = 45$ K, indicating that the lack of a long-range CDW order in FG560 is not due to the mixing of regions with CDW and regions without CDW nor due to low spectral quality from a bad cleavage but a demonstration of a lack of long-range ordering. Below T_{SDW}, a small monotonic energy shift is again observed, also because of the onset of the SDW order as will be discussed later. In Fig. 4F, we summarize the changes in the dispersions along the $\overline{K}$-$\overline{M}$-$\overline{K}$ for FG560.

Intertwined order parameters

We now summarize the temperature dependence of the electronic structure observed on the two types of postannealed FeGe. First, we plot the CDW gap as a function of temperature extracted using the Dynes function (*43*) (fitting details are in the Supplementary Materials) as shown in Fig. 5A. As demonstrated in the earlier section, we identify the onset of the CDW phase in FG320 to be around 110 K, which is consistent with the magnetic susceptibility result in Fig. 1C. When the temperature decreases from T_{CDW}, the CDW gap size reaches 15 meV and then shows an additional increasing behavior below T_{SDW}. For FG560, we observe a similar increasing behavior below 45 K. The fitted results are consistent with the behavior observed directly from symmetrized raw data in Fig. 3 (D and H).

Next, we plot the shift of the Dirac band at the $\overline{K}$ point captured by the shift of the Fermi momentum k_0 (Figs. 5B). Noticeably, for FG320, there is a region showing an abrupt onset at T_{CDW} and its

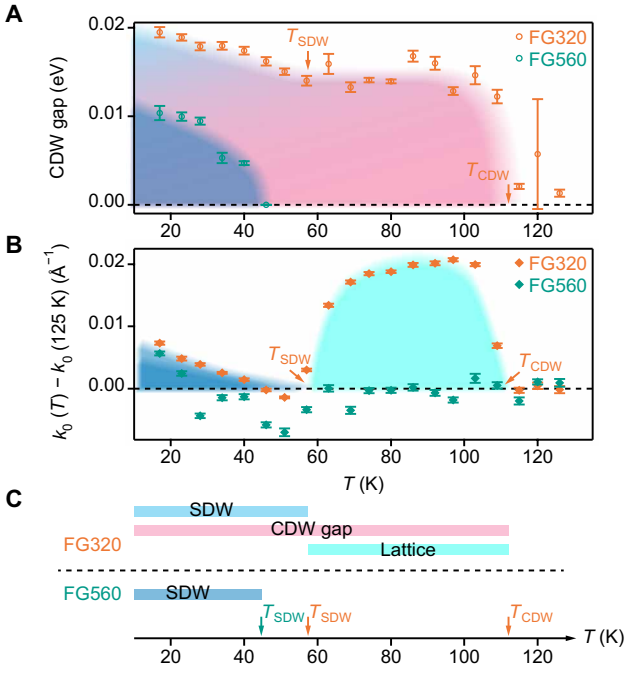

Fig. 5. Summary for the temperature dependence of the electronic structure and intertwined orders. (**A**) CDW gap as a function of temperature measured on FG320 (orange markers) and FG560 (green markers) fitted with the Dynes function (see the Supplementary Materials for details). We mark out regions via the distinct behaviors of the gap as discussed in the main text. (**B**) Shift of the Fermi momentum k_0 as a function of temperature measured for FG320 (orange markers) and FG560 (green markers). (**C**) Distinct regions marked in (A) and (B) from FG320 (top) and FG560 (bottom) are marked with phase indicators (middle) as confirmed by neutron diffraction (*26*) and Raman measurement (*32*).

reversal at T_{SDW}. Such abrupt shift and reversal are absent for FG560. As temperature further decreases, both FG320 and FG560 show a monotonic increasing behavior below T_{SDW}.

On the basis of the two observables presented above for the two types of samples, we discuss the implications. First, the abrupt shift of the Dirac band at T_{CDW} in FG320 has been identified to be due to the electronic response to the abrupt lattice change associated with the Ge dimerization according to density functional theory calculations performed for the fully refined crystal structure and not to CDW gap opening (*38*). The subsequent abrupt reversal at T_{SDW}, therefore, suggests that the electronic response to the lattice distortion is reverted at the onset of the SDW order. This is consistent with a recent x-ray diffraction report showing the disappearance of the lattice dimerization at T_{SDW} (*39*). Note that the abrupt change of k_0 is related to the response of the lattice change but not a direct order parameter of the electronic CDW order as evidenced by a comparison between a topographic image and a dI/dV map (*39*). Second, both annealed crystals exhibit a monotonic shift of the band onset-ting below T_{SDW}. Since the only common phase for the two samples is the SDW order at low temperatures, this must be an electronic response to the SDW order. This band shift is incompatible with the interpretation of this low-temperature magnetic transition as a canting transition, as a simple rotation of local moments has minimal effect on the electronic structure. We confirm this with density functional theory calculations provided in the Supplementary Materials.

Instead, band shift is naturally compatible with an SDW order of itinerant origin. As the bands near E_F are the spin-minority states from the A-type antiferromagnetic (AFM) order (*28*), an upward shift of the bands would suggest an increase in the total magnetic moment. Recently, neutron scattering experiments have revealed that the ordered magnetic moment associated with the A-type AFM order remains constant over this temperature range below T_{CDW} for FG320 (*40*). However, the onset of the SDW order in FG320 adds an increase in the total magnetic moment below T_{SDW}, which is consistent with our understanding that the band shift must be associated with the SDW order, as additional exchange splitting would push the spin-minority bands up in energy. The similar monotonic shift of the bands in both FG320 and FG560 suggests that the SDW order is common between the two annealed crystals, albeit onsetting at a lower temperature in FG560 without the long-range CDW order. Here, we note that the T_{SDW} as detected by neutron diffraction is, in general, associated with the kink feature in the magnetic susceptibility in annealed crystals (Fig. 1C). It is also highly dependent on the annealing condition, typically lower in crystals without a CDW order (*40*). Third, we note that the CDW gap in FG320 is enhanced below T_{SDW}. Even in FG560, the onset of the SDW order seems to result in observable suppression of the spectral weight on the VHS bands at E_F. We interpret this as an enhancement of short-range CDW fluctuations stabilized by the SDW order. In conclusion, the reversed k_0 shift indicates that the change in the lattice degree of freedom across T_{CDW} is reversed across T_{SDW}; meanwhile, the charge degree of freedom still monotonically evolves.

DISCUSSION

From our systematic comparison of the temperature evolution of FG320 and FG560, we come to two key conclusions. First, we discuss the effect of annealing. From our comparison of FG320 and FG560 in the A-type AFM phase above 110 K, the electronic structures of the two crystals are largely identical. This can be best seen in the FS comparison in Fig. 2B and the dispersion comparison in Fig. 2D for 150 K. Comparing the peak width in the MDC at E_F, the peaks are slightly broader in FG560, indicating that the subtle difference may be due to a slightly larger amount of disorder in FG560, as suggested from a previous report (*35*, *37*). In addition, the nearly identical location of the VHSs in the two types of crystals indicates that the VHSs being near E_F by itself is not a sufficient condition for driving the CDW order. The amount of disorder may also play a role. Here, we would like to note that a previous ARPES work concluded that FS nesting does not exist in FeGe based on the autocorrelation of a single FS mapped under one photon polarization (*38*). We would like to caution that the photoemission matrix elements associated with a particular polarization suppress intensity from orbitals of certain symmetries. Hence, the electronic structure including the FS measured under one particular polarization is incomplete. As has already been demonstrated by previous work (*28*), the FSs measured under different polarizations reveal different VHS-associated bands. Hence, the analysis for nesting based on autocorrelation of the measured FS strongly depends on the polarization and is only conclusive when all features are observed. With that said, what we observe here is that although the VHSs are near the E_F here in both types of annealed samples, they are likely not the driving force behind the CDW order in FeGe because long-range order is absent in FG560. As neither the magnetic order nor the electronic structure appears to be strongly tuned by the annealing conditions, this leaves the degree of the lattice disorder to be the most likely key in the annealing process.

Second, from the above analysis of the temperature-dependent evolution of the electronic structure, we reveal an intricate relationship of the lattice, charge, and spin degrees of freedom in FeGe. From FG320, we see that the Ge dimerization is strongly tied to the onset of the CDW order as the gap at k_{VHS} and the Dirac band shift occur simultaneously. In FG560, both are absent. First-principles calculations have demonstrated that the magnetic energy that is gained by the lattice distortion from both the Ge dimerization and the sequential in-plane distortions can overcome the energy cost of the lattice distortion and hence stabilize the 2×2 CDW order (*33*). This would be consistent with our observation of the simultaneous onset of the CDW gap and the band shift. However, the unexpected finding is that this strong coupling between the lattice and charge is abruptly disrupted when the SDW order onsets, as observed in the persistence of the CDW gap while the band shift representing the lattice distortion is suddenly reversed at T_{SDW} in FG320. This suggests that the SDW order appears to replace the lattice distortion in stabilizing the CDW order below T_{SDW}. This reversal of lattice distortion is quite uncommon and is usually accompanied by the onset of another electronic order to account for the entropy. Another example is the hole-doped iron pnictide superconductors, where the lattice exhibits a C_4 to C_2 and back to C_4 rotational symmetry as a function of temperature (*44*, *45*). In that situation, the re-entrant higher-symmetry phase at low temperature is due to the onset of a C_4 double-**Q** SDW order. In the case of FeGe, Raman spectroscopy has reported a lattice symmetry reversal below T_{SDW} (*32*). Here, our observation of the onset of the band shift indicates that the SDW order must provide the additional energy saving that overcomes the energy cost of the lattice distortion. Moreover, our observations suggest that the SDW order can stabilize or enhance the CDW order with minimal effect of the Ge dimerization on the electronic structure, as has been seen below T_{SDW} in FG320 and the gap opening below T_{SDW} in FG560. This is also consistent with the observation that as a function of annealing temperature, the trend of T_{SDW} follows the trend of the enhancement of the CDW order. FG320 with the long-range CDW order at the highest transition temperature also exhibits the highest T_{SDW} (*36*). Hence, the Ge dimerization and the SDW order are strongly coupled to the appearance of the CDW order in FeGe. This cooperation between the lattice, spin, and electronic degrees of freedom in kagome FeGe may hold the key to the tunability of the CDW order in this kagome metal.

MATERIALS AND METHODS

Single-crystal synthesis and postannealing

Single crystals of FeGe were synthesized following the reported recipe using chemical vapor transport (*26*, *28*). We chose 560° and 320°C as the annealing temperatures for our postgrowth annealing protocols, same as the previous reports (*36*). The as-grown crystals were sealed in an evacuated quartz tube and placed in a box furnace and set the temperature to 320°C (FG320). After maintaining this temperature for 96 hours, subsequently, the quartz tube was promptly removed from the furnace and quenched in tap water to room temperature. The same process was repeated for annealing the as-grown FeGe single crystals at 560°C (FG560). The resulting annealed crystals maintain their original lustrous appearance, showing no discernible surface changes due to the annealing process.

Magnetic susceptibility measurement

The magnetization as a function of temperature and field was measured using a Quantum Design DynaCool Physical Properties Measurement System (PPMS-9T) over the temperature range from 2 to 300 K and under 0.1-T magnetic field. Postannealed FG320 and FG560 single crystals were separately mounted on PPMS sample holders, having the crystallographic *c* axis perpendicular to the 0.1-T field. The orientation of the crystal was determined by standard Laue techniques before mounting to PPMS sample holder.

Angle-resolved photoemission spectroscopy

ARPES measurements were carried out at BL5-2 of the Stanford Synchrotron Radiation Lightsource with a DA30 electron analyzer. Postannealed FeGe single crystals were cleaved to have normal surfaces face the (001) direction in ultrahigh vacuum environment with a base pressure better than 5×10^{-11} torr. We identified two different types of termination layer, as our previous study did, and focused on the Ge termination to trace the features from the CDW order more evidently (*28*). Energy and angular resolutions were better than 10 meV and 0.1°, respectively. We adapted beam spot smaller than 50 μm by 50 μm. E_F is corrected by a measurement of freshly deposited gold near crystals, and both are electrically connected, guaranteeing to have the same E_F.

Density functional theory

Electronic structures of FeGe are calculated using density functional theory as implemented in the Vienna Ab initio Simulation Package (*46*). The crystal structure of FeGe is fully relaxed under the AFM configuration until the maximal remaining force is smaller than 1 meV/Å. Spin-orbit coupling is not considered in structure relaxation. The Perdew-Burke-Ernzerhof–type generalized gradient approximation (*47*) mimics the electron-electron exchange interaction throughout. The energy cutoff for the plane wave basis set is 350 eV. Brillouin zones of the AFM and spin-canting phases are sampled with a *k* mesh of $12 \times 12 \times 8$. Band structures are obtained with the spin-orbit coupling.

Supplementary Materials

This PDF file includes:

Supplementary Text
Figs. S1 to S6
References

REFERENCES AND NOTES

1. S. Paschen, Q. Si, Quantum phases driven by strong correlations. *Nat. Rev. Phys.* **3**, 9–26 (2021).
2. E. Dagotto, Complexity in strongly correlated electronic systems. *Science* **309**, 257–262 (2005).
3. E. Fradkin, S. A. Kivelson, J. M. Tranquada, *Colloquium*: Theory of intertwined orders in high temperature superconductors. *Rev. Mod. Phys.* **87**, 457–482 (2015).
4. B. Keimer, J. E. Moore, The physics of quantum materials. *Nat. Phys.* **13**, 1045–1055 (2017).
5. Z. Wang, P. Zhang, Quantum spin Hall effect and spin-charge separation in a kagomé lattice. *New J. Phys.* **12**, 043055 (2010).
6. M. L. Kiesel, R. Thomale, Sublattice interference in the kagome Hubbard model. *Phys. Rev. B* **86**, 121105 (2012).
7. M. L. Kiesel, C. Platt, R. Thomale, Unconventional Fermi surface instabilities in the kagome Hubbard model. *Phys. Rev. Lett.* **110**, 126405 (2013).
8. B. R. Ortiz, L. C. Gomes, J. R. Morey, M. Winiarski, M. Bordelon, J. S. Mangum, I. W. H. Oswald, J. A. Rodriguez-Rivera, J. R. Neilson, S. D. Wilson, E. Ertekin, T. M. McQueen, E. S. Toberer, New kagome prototype materials: Discovery of KV_3Sb_5, RbV_3Sb_5, and CsV_3Sb_5. *Phys. Rev. Mater.* **3**, 094407 (2019).
9. K. Y. Chen, N. N. Wang, Q. W. Yin, Y. H. Gu, K. Jiang, Z. J. Tu, C. S. Gong, Y. Uwatoko, J. P. Sun, H. C. Lei, J. P. Hu, J.-G. Cheng, Double superconducting dome and triple enhancement of T_c in the kagome superconductor CsV_3Sb_5 under high pressure. *Phys. Rev. Lett.* **126**, 247001 (2021).
10. M. M. Denner, R. Thomale, T. Neupert, Analysis of charge order in the kagome metal AV_3Sb_5 (A = K, Rb, Cs). *Phys. Rev. Lett.* **127**, 217601 (2021).
11. Y.-X. Jiang, J.-X. Yin, M. M. Denner, N. Shumiya, B. R. Ortiz, G. Xu, Z. Guguchia, J. He, M. S. Hossain, X. Liu, J. Ruff, L. Kautzsch, S. S. Zhang, G. Chang, I. Belopolski, Q. Zhang, T. A. Cochran, D. Multer, M. Litskevich, Z.-J. Cheng, X. P. Yang, Z. Wang, R. Thomale, T. Neupert, S. D. Wilson, M. Z. Hasan, Unconventional chiral charge order in kagome superconductor KV_3Sb_5. *Nat. Mater.* **20**, 1353–1357 (2021).
12. B. R. Ortiz, P. M. Sarte, E. M. Kenney, M. J. Graf, S. M. L. Teicher, R. Seshadri, S. D. Wilson, Superconductivity in the Z_2 kagome metal KV_3Sb_5. *Phys. Rev. Mater.* **5**, 034801 (2021).
13. H. Zhao, H. Li, B. R. Ortiz, S. M. L. Teicher, T. Park, M. Ye, Z. Wang, L. Balents, S. D. Wilson, I. Zeljkovic, Cascade of correlated electron states in the kagome superconductor CsV_3Sb_5. *Nature* **599**, 216–221 (2021).
14. M. Kang, S. Fang, J.-K. Kim, B. R. Ortiz, S. H. Ryu, J. Kim, J. Yoo, G. Sangiovanni, D. Di Sante, B.-G. Park, C. Jozwiak, A. Bostwick, E. Rotenberg, E. Kaxiras, S. D. Wilson, J.-H. Park, R. Comin, Twofold van Hove singularity and origin of charge order in topological kagome superconductor CsV_3Sb_5. *Nat. Phys.* **18**, 301–308 (2022).
15. M. Kang, S. Fang, J. Yoo, B. R. Ortiz, Y. M. Oey, J. Choi, S. H. Ryu, J. Kim, C. Jozwiak, A. Bostwick, E. Rotenberg, E. Kaxiras, J. G. Checkelsky, S. D. Wilson, J.-H. Park, R. Comin, Charge order landscape and competition with superconductivity in kagome metals. *Nat. Mater.* **22**, 186–193 (2022).
16. Y. Xu, Z. Ni, Y. Liu, B. R. Ortiz, Q. Deng, S. D. Wilson, B. Yan, L. Balents, L. Wu, Three-state nematicity and magneto-optical Kerr effect in the charge density waves in kagome superconductors. *Nat. Phys.* **18**, 1470–1475 (2022).
17. R. Gupta, D. Das, C. H. Mielke III, Z. Guguchia, T. Shiroka, C. Baines, M. Bartkowiak, H. Luetkens, R. Khasanov, Q. Yin, Z. Tu, C. Gong, H. Lei, Microscopic evidence for anisotropic multigap superconductivity in the CsV_3Sb_5 kagome superconductor. *Npj Quantum Mater.* **7**, 49 (2022).
18. Y. Zhong, S. Li, H. Liu, Y. Dong, K. Aido, Y. Arai, H. Li, W. Zhang, Y. Shi, Z. Wang, S. Shin, H. N. Lee, H. Miao, T. Kondo, K. Okazaki, Testing electron–phonon coupling for the superconductivity in kagome metal CsV_3Sb_5. *Nat. Commun.* **14**, 1945 (2023).
19. Y. Zhong, J. Liu, X. Wu, Z. Guguchia, J.-X. Yin, A. Mine, Y. Li, S. Najafzadeh, D. Das, C. Mielke, R. Khasanov, H. Luetkens, T. Suzuki, K. Liu, X. Han, T. Kondo, J. Hu, S. Shin, Z. Wang, X. Shi, Y. Yao, K. Okazaki, Nodeless electron pairing in CsV_3Sb_5-derived kagome superconductors. *Nature* **617**, 488–492 (2023).
20. Y. Hu, X. Wu, A. P. Schnyder, M. Shi, Electronic landscape of kagome superconductors AV_3Sb_5 (A = K, Rb, Cs) from angle-resolved photoemission spectroscopy. *Npj Quantum Mater.* **8**, 67 (2023).
21. S.-K. Jian, Y. Huang, H. Yao, Charge-4*e* superconductivity from nematic superconductors in two and three dimensions. *Phys. Rev. Lett.* **127**, 227001 (2021).
22. X. Xu, J.-X. Yin, Z. Qu, S. Jia, Quantum interactions in topological R166 kagome magnet. *Rep. Prog. Phys.* **86**, 114502 (2023).
23. B. Stenström, L. J. Sundström, Magnetoresistance of hexagonal FeGe single crystals between 4.2 K and 30 K. *Phys. Scr.* **6**, 164–168 (1972).
24. B. Stenström, L. J. Sundström, V. Sagredo, The electrical resistivity of hexagonal FeGe single crystals. *Phys. Scr.* **6**, 209–213 (1972).
25. Y. Jiang, H. Hu, D. Călugăru, C. Felser, S. Blanco-Canosa, H. Weng, Y. Xu, B. A. Bernevig, FeGe as a building block for the kagome 1:1, 1:6:6, and 1:3:5 families: Hidden d-orbital decoupling of flat band sectors, effective models, and interaction Hamiltonians. *Phys. Rev. B* **111**, 125163 (2025).
26. X. Teng, L. Chen, F. Ye, E. Rosenberg, Z. Liu, J.-X. Yin, Y.-X. Jiang, J. S. Oh, M. Z. Hasan, K. J. Neubauer, B. Gao, Y. Xie, M. Hashimoto, D. Lu, C. Jozwiak, A. Bostwick, E. Rotenberg, R. J. Birgeneau, J.-H. Chu, M. Yi, P. Dai, Discovery of charge density wave in a kagome lattice antiferromagnet. *Nature* **609**, 490–495 (2022).
27. J.-X. Yin, Y.-X. Jiang, X. Teng, M. S. Hossain, S. Mardanya, T.-R. Chang, Z. Ye, G. Xu, M. M. Denner, T. Neupert, B. Lienhard, H.-B. Deng, C. Setty, Q. Si, G. Chang, Z. Guguchia, B. Gao, N. Shumiya, Q. Zhang, T. A. Cochran, D. Multer, M. Yi, P. Dai, M. Z. Hasan, Discovery of charge order and corresponding edge state in kagome magnet FeGe. *Phys. Rev. Lett.* **129**, 166401 (2022).
28. X. Teng, J. S. Oh, H. Tan, L. Chen, J. Huang, B. Gao, J.-X. Yin, J.-H. Chu, M. Hashimoto, D. Lu, C. Jozwiak, A. Bostwick, E. Rotenberg, G. E. Granroth, B. Yan, R. J. Birgeneau, P. Dai, M. Yi, Magnetism and charge density wave order in kagome FeGe. *Nat. Phys.* **19**, 814–822 (2023).
29. Y.-P. Lin, C. Liu, J. E. Moore, Complex magnetic and spatial symmetry breaking from correlations in kagome flat bands. *Phys. Rev. B* **110**, L041121 (2024).
30. H. Miao, T. T. Zhang, H. X. Li, G. Fabbris, A. H. Said, R. Tartaglia, T. Yilmaz, E. Vescovo, J.-X. Yin, S. Murakami, X. L. Feng, K. Jiang, X. L. Wu, A. F. Wang, S. Okamoto, Y. L. Wang, H. N. Lee, Signature of spin-phonon coupling driven charge density wave in a kagome magnet. *Nat. Commun.* **14**, 6183 (2023).

31. L. Chen, X. Teng, H. Tan, B. L. Winn, G. E. Granroth, F. Ye, D. H. Yu, R. A. Mole, B. Gao, B. Yan, M. Yi, P. Dai, Competing itinerant and local spin interactions in kagome metal FeGe. *Nat. Commun.* **15**, 1918 (2024).
32. S. Wu, M. L. Klemm, J. Shah, E. T. Ritz, C. Duan, X. Teng, B. Gao, F. Ye, M. Matsuda, F. Li, X. Xu, M. Yi, T. Birol, P. Dai, G. Blumberg, Symmetry breaking and ascending in the magnetic kagome metal FeGe. *Phys. Rev. X* **14**, 011043 (2024).
33. Y. Wang, Enhanced spin-polarization via partial Ge1-dimerization as the driving Force of the 2×2×2 CDW in FeGe. *Phys. Rev. Mater.* **7**, 104006 (2023).
34. S. Yi, Z. Liao, Q. Wang, H. Ma, J. Liu, X. Teng, B. Gao, P. Dai, Y. Dai, J. Zhao, Y. Qi, B. Xu, X. Qiu, Charge dynamics of an unconventional three-dimensional charge density wave in kagome FeGe. *Phys. Rev. Lett.* **134**, 086902 (2025).
35. Z. Chen, X. Wu, S. Zhou, J. Zhang, R. Yin, Y. Li, M. Li, J. Gong, M. He, Y. Chai, X. Zhou, Y. Wang, A. Wang, Y.-J. Yan, D.-L. Feng, Discovery of a long-ranged charge order with 1/4 Ge1-dimerization in an antiferromagnetic kagome metal. *Nat. Commun.* **15**, 6262 (2024).
36. X. Wu, X. Mi, L. Zhang, C.-W. Wang, N. Maraytta, X. Zhou, M. He, M. Merz, Y. Chai, A. Wang, Annealing-tunable charge density wave in the magnetic kagome material FeGe. *Phys. Rev. Lett.* **132**, 256501 (2024).
37. C. Shi, Y. Liu, B. B. Maity, Q. Wang, S. R. Kotla, S. Ramakrishnan, C. Eisele, H. Agarwal, L. Noohinejad, Q. Tao, B. Kang, Z. Lou, X. Yang, Y. Qi, X. Lin, Z.-A. Xu, A. Thamizhavel, G.-H. Cao, S. Van Smaalen, S. Cao, J.-K. Bao, Annealing-induced long-range charge density wave order in magnetic kagome FeGe: Fluctuations and disordered structure. *Sci. China Phys. Mech. Astron.* **67**, 117012 (2024).
38. Z. Zhao, T. Li, P. Li, X. Wu, J. Yao, Z. Chen, Y. Yan, S. Cui, Z. Sun, Y. Yang, Z. Jiang, Z. Liu, A. Louat, T. Kim, C. Cacho, A. Wang, Y. Wang, D. Shen, J. Jiang, D. Feng, Photoemission evidence of a novel charge order in kagome metal FeGe. *Sci. China Phys. Mech. Astron.* **68**, 267012 (2025).
39. C. Shi, H. Deng, S. R. Kotla, Y. Liu, S. Ramakrishnan, C. Eisele, H. Agarwal, L. Noohinejad, J.-Y. Liu, T. Yang, G. Liu, B. B. Maity, Q. Wang, Z. Lin, B. Kang, Y. Li, Z. Yang, Y. Li, Y. Qi, W. Ren, G.-H. Cao, J.-X. Yin, S. van Smaalen, S. Cao, Charge density wave without long-range structural modulation in canted antiferromagnetic kagome FeGe. arXiv:2404.00996 [cond-mat.str-el] (2024).
40. M. L. Klemm, S. Siddique, Y.-C. Chang, S. Xu, Y. Xie, T. Legvold, M. T. Kiani, X. Teng, B. Gao, F. Ye, H. Cao, Y. Hao, W. Tian, H. Luetkens, M. Matsuda, D. Natelson, Z. Guguchia, C.-L. Huang, M. Yi, J. J. Cha, P. Dai, Vacancy-induced suppression of charge density wave order and its impact on magnetic order in kagome antiferromagnet FeGe. *Nat. Commun.* **16**, 3313 (2025).
41. H. Tan, B. Yan, Disordered charge density waves in the kagome metal FeGe. *Phys. Rev. B* **111**, 045160 (2025).
42. M. Wenzel, E. Uykur, A. A. Tsirlin, S. Pal, R. M. Roy, C. Yi, C. Shekhar, C. Felser, A. V. Pronin, M. Dressel, Intriguing low-temperature phase in the antiferromagnetic kagome metal FeGe. *Phys. Rev. Lett.* **132**, 266505 (2024).
43. R. C. Dynes, V. Narayanamurti, J. P. Garno, Direct measurement of quasiparticle-lifetime broadening in a strong-coupled superconductor. *Phys. Rev. Lett.* **41**, 1509–1512 (1978).
44. S. Avci, O. Chmaissem, J. M. Allred, S. Rosenkranz, I. Eremin, A. V. Chubukov, D. E. Bugaris, D. Y. Chung, M. G. Kanatzidis, J.-P. Castellan, J. A. Schlueter, H. Claus, D. D. Khalyavin, P. Manuel, A. Daoud-Aladine, R. Osborn, Magnetically driven suppression of nematic order in an iron-based superconductor. *Nat. Commun.* **5**, 3845 (2014).
45. A. E. Böhmer, F. Hardy, L. Wang, T. Wolf, P. Schweiss, C. Meingast, Superconductivity-induced re-entrance of the orthorhombic distortion in $Ba_{1-x}K_xFe_2As_2$. *Nat. Commun.* **6**, 7911 (2015).
46. G. Kresse, J. Furthmüller, Efficient iterative schemes for *ab initio* total-energy calculations using a plane-wave basis set. *Phys. Rev. B* **54**, 11169–11186 (1996).
47. J. P. Perdew, K. Burke, M. Ernzerhof, Generalized gradient approximation made simple. *Phys. Rev. Lett.* **77**, 3865–3868 (1996).

Acknowledgments

Funding: Use of the Stanford Synchrotron Radiation Lightsource, SLAC National Accelerator Laboratory, is supported by the US Department of Energy (DOE), Office of Science, Office of Basic Energy Sciences (BES) under contract no. DE-AC02-76SF00515. The ARPES work at Rice University was supported by the Gordon and Betty Moore Foundation's EPiQS Initiative through grant no. GBMF9470 and the Robert A. Welch Foundation grant no. C-2175 (to M.Y.). This research was supported by Sookmyung Women's University Research grant no. 1-2403-2026 (to J.S.O.). The single-crystal synthesis and characterization work at Rice University was supported by the US National Science Foundation DMR-2401084, DMR-2302420, and the Robert A. Welch Foundation grant no. C-1839 (to P.D.). Work at the University of California, Berkeley and Lawrence Berkeley National Laboratory was funded by the US DOE, Office of Science, BES, Materials Sciences and Engineering Division under contract no. DE-AC02-05CH11231 (Quantum Materials Program KC2202) (to R.J.B.). We acknowledge the support from National Science Foundation grants nos. DMR-2324035 and DMR-2324032 (to J.S.O., R.J.B., and M.Y.). M.H. and D.L. acknowledge the support of the U.S. Department of Energy, Office of Science, Office of Basic Energy Sciences, Division of Material Sciences and Engineering, under Contract No. DE-AC02-76SF00515. **Author contributions:** Conceptualization: J.S.O., P.D., and M.Y. Methodology: J.S.O., A.B., M.L.K., Y.X., B.G., M.H., D.L., P.D., and M.Y. Investigation: J.S.O., A.B., M.L.K., Y.X., B.G., H.T., and M.Y. Visualization: J.S.O. and A.B. Supervision: B.Y., P.D., R.J.B., and M.Y. Writing—original draft: J.S.O. and M.Y. Writing—review and editing: J.S.O., A.B., M.L.K., H.T., Y.X., B.G., M.H., D.L., B.Y., P.D., R.J.B., and M.Y. **Competing interests:** The authors declare that they have no competing interests. **Data and materials availability:** All data needed to evaluate the conclusions in the paper are present in the paper and/or the Supplementary Materials.

Submitted 17 September 2024
Accepted 28 May 2025
Published 2 July 2025
10.1126/sciadv.adt2195